Clinical Radiology 74 (2019) 165.e1–165.e9

Contents lists available at ScienceDirect

Clinical Radiology

journal homepage: www.clinicalradiologyonline.net

Utility of arterial spin labelling MRI for discriminating atypical high-grade glioma from primary central nervous system lymphoma

N. Di [a,b], W. Cheng [c], H. Chen [d], F. Zhai [a], Y. Liu [e], X. Mu [a], Z. Chu [a], N. Lu [b], X. Liu [a,*], B. Wang [f,*]

[a] Department of Radiology, Binzhou Medical University Hospital, 661 Huanghe 2nd Rd, 256603 Binzhou, China
[b] Department of Radiology, Huashan Hospital Fudan University, 12 Wulumuqi Rd. Middle, 200040 Shanghai, China
[c] Department of Pharmacy, Binzhou Medical University Hospital, 661 Huanghe 2nd Rd, 256603 Binzhou, China
[d] Department of Radiology, Weifang Traditional Chinese Hospital, 1055 Weizhou Rd, 261000 Weifang, China
[e] Department of Pediatrics, Binzhou Medical University Hospital, 661 Huanghe 2nd Rd, 256603 Binzhou, China
[f] Department of Medical Imaging and Nuclear, Binzhou Medical University, 346 Guanhai Rd, 264000 Yantai, China

ARTICLE INFORMATION

Article history:
Received 2 February 2018
Accepted 9 October 2018

AIM: To evaluate the ability of arterial spin labelling (ASL) magnetic resonance imaging (MRI) in differentiating primary central nervous system lymphoma (PCNSL) from atypical high-grade glioma (HGG), as well as exploring the underlying pathological mechanisms.

METHODS AND MATERIALS: Twenty-three patients with PCNSL and 17 patients with atypical HGG who underwent ASL-MRI were identified retrospectively. Absolute cerebral blood flow (aCBF) and normalised cerebral blood flow (nCBF) values were obtained, and were compared between PCNSL and atypical HGG using the Mann–Whitney *U*-test. The performance in discriminating between PCNSL and atypical HGG was evaluated using receiver-operating characteristics analysis and area-under-the-curve (AUC) values for aCBF and nCBF. The correlation between microvessel density (MVD) and aCBF was determined by Spearman's correlation analysis.

RESULTS: Atypical HGG demonstrated significantly higher aCBF, nCBF, and MVD values than PCNSL ($p<0.05$). The diagnostic accuracy of discriminating PCNSL from atypical HGG showed AUC=0.877 (95% confidence interval [CI] 0.735–0.959) for aCBF, and AUC=0.836 (95% confidence interval [CI] 0.685–0.934) for nCBF. There was a moderate positive correlation between aCBF values of region of interest (ROI >30 mm^2) in the enhanced area and MVD values (rho=0.579, $p=0.0001$), and a strong positive correlation between aCBF values MVD based on "point-to-point biopsy" (rho=0.83, $p=0.0029$). Interobserver agreements for aCBF and nCBF were excellent (ICC >0.75).

CONCLUSIONS: ASL perfusion MRI is a useful imaging technique for the discrimination between atypical HGG and PCNSL, which may be determined by the difference of MVD between them.

* Guarantor and correspondent: B. Wang, Department of Medical Imaging and Nuclear, Binzhou Medical University, 346 Guanhai Rd, 264000 Yantai, China. Tel.: +86 15905350169; fax: +86 0535 6913002., X. Liu, Department of Radiology, Binzhou Medical University Hospital, 661 Huanghe 2nd Rd, 256603 Binzhou, China. Tel.: +86 13356286368; fax: +86 0543 3256590.
E-mail addresses: binwang001@aliyun.com (B. Wang), lxj6513@163.com (X. Liu).

https://doi.org/10.1016/j.crad.2018.10.003
0009-9260/

Introduction

High-grade glioma (HGG) is the most common primary malignant brain tumour in adults with high lethality and recurrence rate. Gross surgical resection followed by chemoradiation using temozolomide or anti-angiogenesis therapy is needed for the treatment of HGG. In contrast, primary central nervous system lymphoma (PCNSL) is less common than HGG, and is usually diagnosed by a targeted biopsy and treated with chemotherapy and radiotherapy.[1,2] It is clear that pretreatment differentiation between HGG and PCNSL is essential for therapeutic decision-making.

Routine morphological contrast-enhanced (CE) T1-weighted imaging (WI) has been used to differentiate PCNSL from HGG in many cases as HGG typically shows a heterogeneous enhancement and necrosis, but PCNSL typically shows homogeneous enhancement[3,4]; however, atypical HGG lesions showing no necrosis may complicate the discrimination of HGG from PCNSL on conventional magnetic resonance imaging (MRI).[5] Histologically, the tumour vascular microenvironments of PCNSL and HGG differ. Decreased tumour blood perfusion and increased vascular permeability are more often observed in PCNSL in contrast to HGG.[6–8] Information on tumour haemodynamics can be determined with various MRI techniques. Numerous studies have applied dynamic susceptibility CE (DSC) and dynamic CE (DCE) imaging, both of which are gadolinium-based contrast agent (GBCA)-enhanced MRI perfusion techniques, to differentiate PCNSL from HGG[7–14]; however, an association between GBCA-enhanced MRI results and nephrogenic systemic fibrosis was observed in patients with normal or impaired renal function.[15,16] Additionally, a series of reports have confirmed long-term gadolinium retention in the central nervous system and skin of patients who underwent GBCA-enhanced examinations.[17–20] Patient safety concerns regarding the use of GBCAs should be noted when performing CE examinations. Finally, perfusion parameters can be biased differently on T1and T2* images due to contrast agent leakage from the tumour vasculature.

Arterial spin labelling (ASL) is a promising perfusion MRI technique that quantifies blood flow in tissues by magnetically labelling arterial water as an endogenous diffusible tracer.[21] Compared with DCE and DSC perfusion, ASL-MRI is a contrast-independent technique, avoiding the safety concerns of GBCAs and has an increased resistance to contrast medium leakage effects. ASL scans can be acquired in 4.5 minutes with high reliability and reproducibility, allowing widespread clinical application.[22,23] Several studies have demonstrated the ability of ASL-MRI to differentiate HGG from PCNSL[24–26]; however, most of these studies enrolled patients with HGGs or PCNSLs as a single study cohort, regardless of their findings on conventional MRI. Additionally, a correlation between ASL-MRI perfusion values and the microvascular environment of histological specimens in atypical HGG and PCNSL has not been determined to the authors' knowledge.

This retrospective study focused on atypical HGGs and PCNSLs showing no macroscopic necrosis in the enhanced tumour. The aims were to determine the potential of ASL-MRI in the differentiation of atypical HGG and PCNSL and explore the pathological mechanism by comparing ASL absolute cerebral blood flow (aCBF) and microvessel density (MVD).

Materials and methods

Patients

This retrospective study was approved by the institutional review board, which waived the requirement for informed consent. A total of 156 cases with HGG (anaplastic astrocytoma=85 and glioblastoma multiforme =71) and 31 cases with PCNSL who underwent preoperative ASL-MRI from August 2015 to June 2018 were reviewed retrospectively. The inclusion criteria for atypical HGG and PCNSL were: (1) enhancing lesions showing no visual necrosis on CE T1WI, (2) no prior biopsy or pre-treatment or history of primary tumour of other organs, and (3) preoperative ASL-MRI with no motion artefacts. Finally, a total of 40 intra-axial brain tumour patients with 17 atypical HGGs (anaplastic astrocytoma, n=12; glioblastoma, n=5) and 23 cases with PCNSL (diffuse large B-cell lymphoma) were analysed.

MRI techniques

MRI was performed using a 3.0T MRI system (Discovery MR750, GE Medical Systems, Milwaukee, WI, USA) with an eight-channel phased-array coil. The preoperative MRI protocol included an acquisition of T1WI (repetition time [TR]=1,980 ms, echo time [TE]=19 ms, field of view [FOV]=24×24 cm, section thickness=4 mm, number of excitations [NEX]=1, matrix=256×256), T2WI (TR=8,200 ms, TE=90 ms, FOV=240 mm, section thickness=4 mm, NEX=2, matrix=256×256), and T2 fluid-attenuated inversion recovery (FLAIR) images (TR=9,000 ms, TE=135 ms, FOV=240 mm, section thickness=1.5 mm, NEX=1, matrix=256×256). ASL scans were obtained by using a pseudocontinuous pulse sequence with background-suppressed three-dimensional (3D) gradient and spin-echo readout (FOV=24×24 cm, TR=4527 ms, TE=10.5 ms, section thickness=4 mm, NEX=3, post-label delay=1,525 ms, and scan time=4 minutes 23 seconds). When the ASL scans finished, 3D T1BRAVO C+ images (TR=6.3 ms, TE=3.1 ms, FOV=240 mm, section thickness=1 mm, NEX=1, matrix=256×256) were acquired after a bolus of 0.1 mmol/kg of Gd-DTPA (Omniscan; GE Healthcare, Cork, Ireland) was injected at a rate of 3.5 ml/s using a power injector via an intravenous catheter placed in the left or right antecubital vein, followed by a 15 ml saline flush.

Point-to-point biopsy

Nine cases (atypical HGG=4, PCNSL=5) underwent point-to-point stereotactic biopsy based on real-time intraoperative MRI (iMRI). During this procedure, firstly, preoperative 3D T1C+ images were loaded onto a Mei De

medical workstation (SINORAO; Shenzhen, China), and the cannula entry point, trajectory, and biopsy target (size=10×10 mm) were established. Then, the 3D T1C+ images labelled with the pre-planned biopsy target were sent to the workstation of the neuro-navigation system (StealthStation TREON; Medtronic, Minneapolis, MN, USA). Under the guidance of iMRI, a ferromagnetic, passively navigated, 2.2×9 mm side-cut biopsy needle (Medtronic) was used to obtain samples within the targeted regions of interest (ROI) using the navigation system (Medtronic StealthStation i7 Integrated Navigation System, Canada). After completing the biopsy core sampling, the biopsy needle was left in place for at least 5 minutes to promote haemostasis. The biopsy procedure was considered complete after the biopsied tissue provided a definitive diagnosis.

MRI data analysis

The AW4.6 workstation (GE Healthcare, Milwaukee, WI, USA) was used to perform CBF measurements. For each tumour, a mean aCBF was measured in a circular ROI (area >30 mm^2) that was placed on the CBF maps within the area that corresponded to the enhancing area on the CE T1WI images. Regions with relatively high CBF were targeted, while careful attention was paid to avoid contamination of blood vessels, calcification, necrosis, and haemorrhage for ROI placement (Fig 1). For tumours with point-to-point biopsy, a ROI was first manually drawn on the contrast-enhanced T1 WI images according to the biopsy target area, and then co-registered onto the ASL derived CBF maps to obtain CBF values (Figs 2 and 3). In addition, to minimise variances in the aCBF value in an individual patient, the normalised CBF (nCBF) was calculated by dividing the aCBF values from ROI of the tumour by the mean CBF value from a ROI (>30 mm^2) in the contralateral unaffected white matter. Each aCBF or nCBF was measured by three different neuroradiologists; the mean of three measurements determined the final aCBF or nCBF values.

Histopathological evaluation

Biopsy and surgically removed tissues were fixed in 10% formalin, embedded in paraffin, and cut into 4-μm specimens

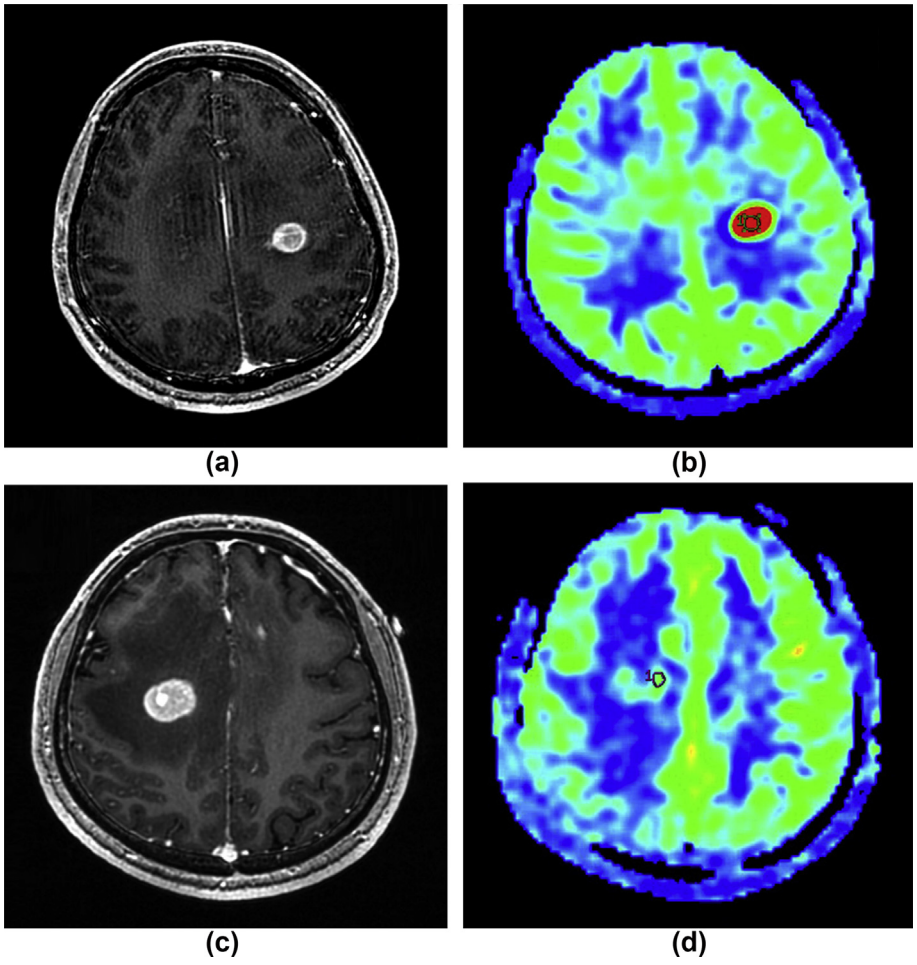

Figure 1 MRI images of (a–b) anaplastic astrocytoma located in the left frontal lobe of a 39-year-old male patient and (c–d) PCNSL located in the right frontal lobe of a 50-year-old male patient. Both masses show solid enhancement with no visual necrosis and on axial 3D T1C+ (a, c) images. ROIs of >30 mm^2 were placed within the most intense area in the ASL-derived CBF maps corresponding to the enhancing portion of the tumour and the aCBF values were measured (b, d).

for histopathological analysis. All specimens were examined under a light microscope. Sections for CD34 staining (Changdao, Shanghai, China) did not require antigen retrieval, but were incubated for 26 minutes. Visualisation was completed with a streptavidin–biotin–horseradish peroxidase system, with diaminobenzidine as a chromogen. Sections were counterstained in haematoxylin. MVD was determined on the basis of CD34 immunostaining. Briefly, 3–5 areas with high microvascular attenuation on CD34-stained sections were identified at ×200 magnification. MVDs consisting of endothelium and vessel lumen were quantified in the selected area. The criteria established by Weidner were used for counting vessels.[27] Results were expressed as the mean of the 3–5 areas of MVD for each sample.

Statistical analysis

The Bland–Altman analysis and the intraclass correlation coefficient (ICC) were used to assess the relative agreement between the aCBF and nCBF values of every two observer s. ICC values of ≤0, 0–0.39, 0.40–0.59, 0.60–0.74, and >0.75 indicated negative, poor, fair, good, and excellent agreement, respectively. The Mann–Whitney *U*-test was performed to compare the aCBF, nCBF, and MVD values between PCNSL and atypical HGG. The diagnostic accuracy of aCBF and nCBF for differentiating PCNSL from HGG was determined by the receiver-operating characteristics (ROC) analysis with calculation of area under the ROC curve (AUC) values, sensitivity, specificity, optimal cut-off value. AUC values were compared with each other using a non-parametric approach. The correlation between aCBF and MVD was determined by Spearman's correlation coefficient analysis. All statistical analyses were performed using Medcalc, version 15.10. A p-value <0.05 was considered statistically significant.

Results

Bland–Altman plots and ICC demonstrated excellent reliability and reproducibility of aCBF and nCBF measurements between observers 1 and 2, observers 1 and 3, and observers 2 and 3. Correspondingly, the mean biases were −4.6, −3.7, and 0.6 (ml/100 g/min) with 95% limits of agreement of −21 to 11.7, −22.5 to 15.1, and −28.6 to 29.9 (ml/100 g/min) for the aCBF value. For nCBF value, the mean biases were 0.21, 0.09 and −0.1 (ml/100 g/min) with 95% limits of agreement of −1.02 to 1.43, −1.35 to 1.53 and −2.1 to 1.8 (ml/100 g/min; Fig 4). Meanwhile, the ICC was

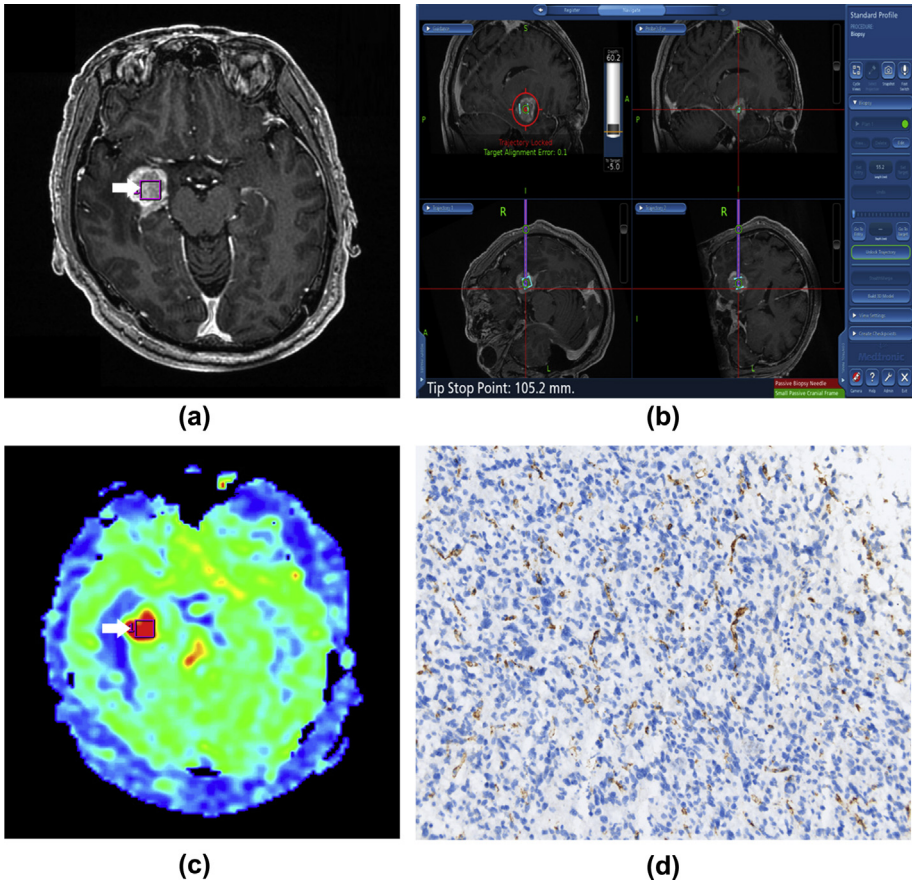

Figure 2 A 63-year-old male patient with anaplastic astrocytoma located in the right temporal lobe. (a) One ROI is pre-established by the hyperenhancement and defined as the biopsy target from 3D T1C+ image (arrow). (b) Biopsy sample within the ROI is obtained using the neuronavigation system. (c) The co-registered ROIs show a high CBF on the map (arrow). (d) The corresponding biopsy specimen shows high MVD (magnification ×200).

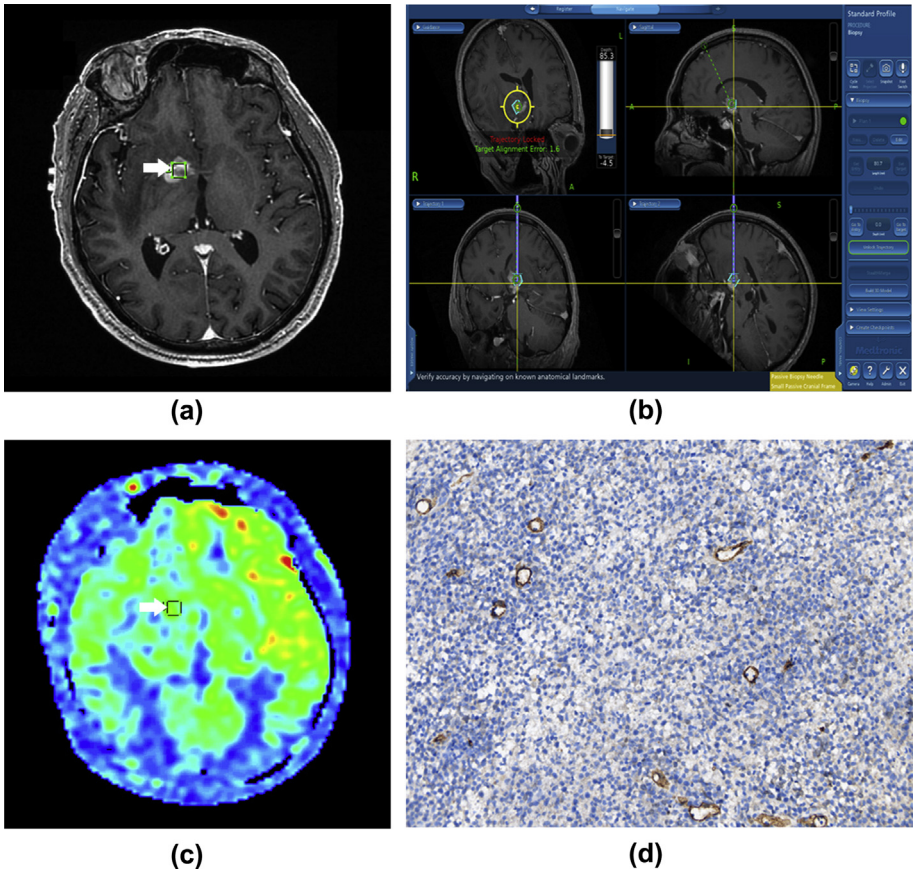

Figure 3 A 62-year-old male patient with PCNSL located in right basal ganglia. (a) One ROI is pre-established by the hyper-enhancement and defined as the biopsy target from 3D T1C+ image (arrow). (b) Biopsy sample within the ROI is obtained using the neuro-navigation system. (c) The co-registered ROIs show relative low CBF on the map (arrow). (d) The corresponding biopsy specimen shows low MVD (magnification ×200).

observed to be 0.97 (95% confidence interval [CI]: 0.945 to 0.984), 0.962 (95% CI: 0.93 to 0.979), and 0.948 (95% CI: 0.906 to 0.972) for aCBF, and 0.901 (95% CI: 0.823 to 0.949), 0.838 (95% CI: 0.726 to 0.906), and 0.768 (95% CI: 0.555 to 0.896) for nCBF, respectively.

The aCBF, nCBF, and MVD values tended to be distributed in significantly higher values in atypical HGG than in PCNSL: 100.53±35.15 versus 55.49±26.61 (p=0.0001), 3.73±1.25 versus 2.35±1.02 (p=0.0003), 58.43±16.48 versus 28.01±11.00 (p<0.0001). These results are summarised in Table 1 and Fig 5. Representative cases of CBF maps and MVD of PCNSL and atypical HGG are presented in Figs 1–3.

The results of the diagnostic performance of the aCBF and nCBF values for differentiating PCNSL from atypical HGG are summarised in Table 2 and Fig 6. Based on ROC analysis, the AUCs were 0.877 (95% CI: 0.735 to 0.959) for aCBF and 0.836 (95% CI: 0.685 to 0.934) for nCBF. The aCBF cut-off value of <62.3 indicated PCNSL with a specificity of 90.48% and sensitivity of 68.82%, and the nCBF cut-off value of <2.396 indicated PCNSL with a specificity of 88.24% and sensitivity of 69.57%. No significant difference in AUC values was found between aCBF and rCBF measurements (p>0.05).

A moderate correlation was found between the ASL-derived aCBF and MVD values (rho=0.579; p=0.0001; Fig 7a). Interestingly, based on the "point-to-point biopsy" subsequent study, a strong positive correlation was found between aCBF and MVD (rho=0.83; p=0.0029; Fig 7b).

Discussion

The present study evaluated the diagnostic performance of ASL MRI-derived aCBF and nCBF values in preoperative differentiation of atypical HGG and PCNSL and explored the pathological mechanism by comparing ASL-derived aCBF values with the microvascular marker, MVD. These results demonstrated that ASL-MRI could be a useful imaging technique for discriminating atypical HGG from PCNSL, which may be determined by the difference of MVD between them.

MR perfusion imaging plays an important role in the differentiation between PCNSL and HGG owning to their differing haemodynamics. Two major perfusion MRI techniques using gadolinium-based contrast agents, DSC-MRI and DCE-MRI, have been widely used to differentiate the two tumours. It has reported that CBV based on DSC-MRI in the enhancing portion of PCNSL had a significantly lower value than that of HGG and showed a high diagnostic

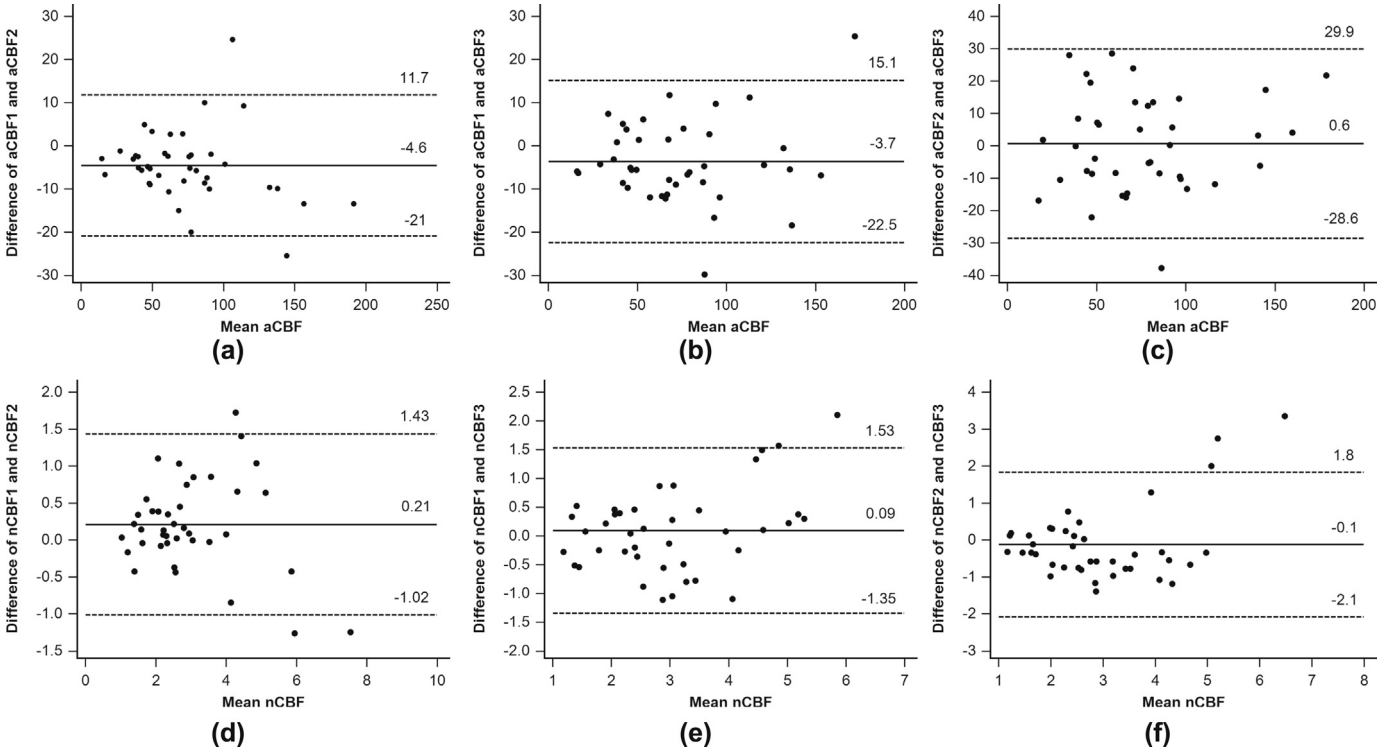

Figure 4 Bland–Altman plots of the difference between aCBF and nCBF measured by every two observers. aCBF1/nCBF1, aCBF2/nCBF2, and aCBF3/nCBF3 represent aCBF/nCBF values measured by observers 1, 2, and 3, respectively. Broken and continuous lines indicate mean difference and 95% limits of agreement (mean difference ±1.96 standard deviation of the paired difference).

accuracy of AUC=0.984.[9] Based on DCE-MRI, the semi-quantitative parameter initial AUC (IAUC), or the quantitative parameters including volume transfer constant (K^{trans}) and volume of extravascular extracellular space (Ve) and volume of vascular plasma space (Vp) also showed good diagnostic performances in differentiating PCNSL from HGG (AUC: IAUC=0.866, K^{trans}=0.847, Ve=0.785, Vp=0.728)[12–14]; however, DSC and DCE MR perfusion techniques need gadolinium-based contrast agents. These perfusion parameters may be affected by T2* and T1 shortening effect due to gadolinium-based contrast media leakage.[28] As an alternative to MR perfusion techniques, ASL-MRI requires no extrinsic tracer or radiation exposure, which is an advantage over other perfusion imaging techniques. In addition, ASL-CBF does not need complicated post-processing compared with DCE-derived quantified parameters, and has a lower susceptibility artefact score than DSC-MRI.[29,30]

Thereby, ASL-MRI has been reported as a vital tool for differentiating HGG from PCNSL using varied CBF quantitative analyses.[24–26] By measuring tumour blood flow (TBF) on ASL perfusion maps at five ROIs, randomly selected within the area corresponding to the enhancing portion of the tumour, Yoo *et al.*[24] demonstrated the potential of absolute TBF (aTBF) and normalised $TBF_{contralateral\_WM}$ ($nTBF_{contralateral\_GM}$=aTBF/$TBF_{contralateral\_GM}$, $TBF_{contralateral\_GM}$: the TBF of contralateral grey matter) in discriminating between HGG and PCNSL, with a sensitivity (100%, 55.6%) and specificity (65%, 100%), respectively. In another method, quantifying ASL-derived aTBF within the entire enhancing portion of each tumour and the responding $nTBF_{contralateral\_WM}$ ($nTBF_{contralateral\_WM}$=aTBF/$TBF_{contralateral\_WM}$, $TBF_{contralateral\_WM}$: the TBF of contralateral white matter), Yamashita *et al.*[25] demonstrated that the AUC for aTBF and nTBF values were 0.888 and 0.810. Recently, You *et al.*[26] measured aTBF,

Table 1
Comparisons of quantitative analysis of absolute cerebral blood flow (aCBF), normalised cerebral blood flow (nCBF) and microvessel density (MVD) between atypical high-grade glioma (HGG) and primary central nervous system lymphoma (PCNSL).

	HGG		PCNLS		*p*-Value
	Mean±SD	Median (range)	Mean±SD	Median (range)	
aCBF (ml/100 g/min)	100.53±35.15	92.66 (48.11–180.70)	55.49±26.61	48.79 (16.04–140.29)	0.0001
nCBF	3.73±1.25	3.55 (2.26–6.62)	2.35±1.02	2.16 (1.06–5.26)	0.0003
MVD	58.43±16.48	52.88 (40.73–89.23)	28.01±11.00	25.65 (12.95–58.72)	<0.001

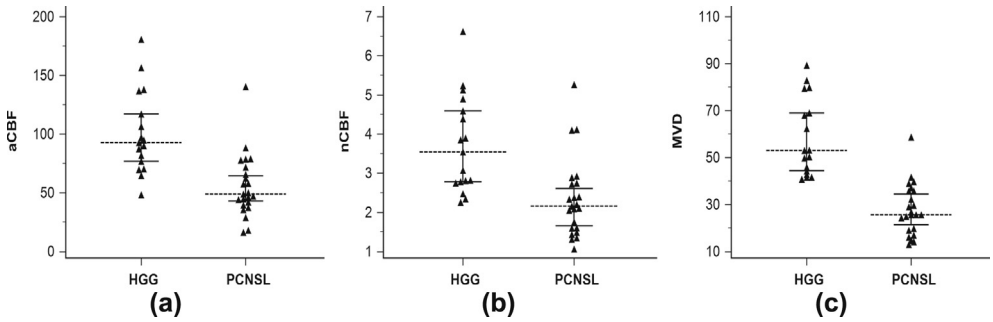

Figure 5 Plots of aCBF, nCBF, and MVD in atypical HGG and PCNSL. The aCBF, nCBF, and MVD are significantly higher in atypical HGG higher than PCNSL ($p<0.001$).

Table 2
Diagnostic accuracy of quantitative analysis of arterial spin labelling (ASL)-driven cerebral blood flow for differentiating atypical high-grade glioma (HGG) from primary central nervous system lymphoma (PCNSL).

	AUC (95%CI)	Sensitivity (%)	Specificity (%)	Cut-off value	Youden index J	*p*-Value
aCBF	0.877 (0.735–0.959)	90.48	68.82	62.30	0.637	<0.001
nCBF	0.836 (0.685–0.934)	88.24	69.57	2.396	0.578	<0.001

$nTBF_{contralateral\_GM}$, and $nTBF_{contralateral\_WM}$ within the most intense area seen in the ASL map corresponding to the enhancing portion of the tumour in CE T1WI, showing diagnostic performance with AUCs of 0.764, 0.849, and 0.795, respectively. This confirmed the good diagnostic performance of ASL-MRI in differentiating PCNSL from HGG.

Similar to the method described in the study conducted by You *et al.*,[26] the present study measured the aCBF of the most intense area (ROI >30 mm^2) on the ASL-CBF map and also gained nCBF by dividing aCBF by CBF of the contralateral white matter. Similarly, good diagnostic accuracy of aCBF and nCBF for discriminating PCNSL from HGG was also demonstrated with AUCs of 0.877 and 0.836, respectively; however, previous studies enrolled all PCNSL and HGG cases, regardless of atypical or typical cases, which may have confounded conventional MRI findings. Thus, it was reasonable for this study to focus on atypical HGG and PCNSL cases to better determine if the ASL perfusion technique is practical for discriminating PCNSL from HGG.

In addition, the present study compared aCBF values with the tumour vascularity marker, MVD, to explore the pathological mechanistic differences of aCBF between PCNSL and HGG. The radiological–pathological correlation studied here has not been elucidated in previous studies. A higher MVD was observed in HGG compared with PCNSL, corresponding to the differing microvascular environments. Specifically, HGG showed increased angiogenesis activity compared with PCNSL.[7] The positive correlation between aCBF and MVD was confirmed in this study, implying that the ASL-derived aCBF value may be directly related to the MVD in tumours. This was similar to the result of our previous study which focused on pure gliomas.[31] Differently, the present study enrolled mixed brain tumor (including HGG and PCNSL). The positive correlation may better demonstrate the role of MVD in determining ASL-derived CBF, regardless of tumor pathologic status. Such positive correlation was supported by the results of Dangouloff-Ros *et al.* who found that the tumour area with high aCBF value tended to show relatively high MVD, regardless of tumour grade for some cases.[32] In another study conducted by Yamamoto T et al.[33], a strong positive correlation between MVD and TBF in parotid region tumors included Warthin

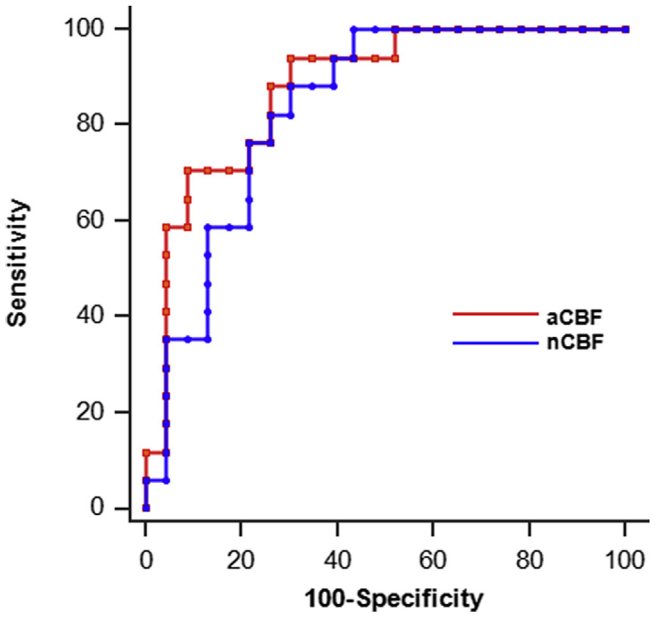

Figure 6 ROC curve of the ASL-derived CBF for differentiating between atypical HGG and PCNSL.

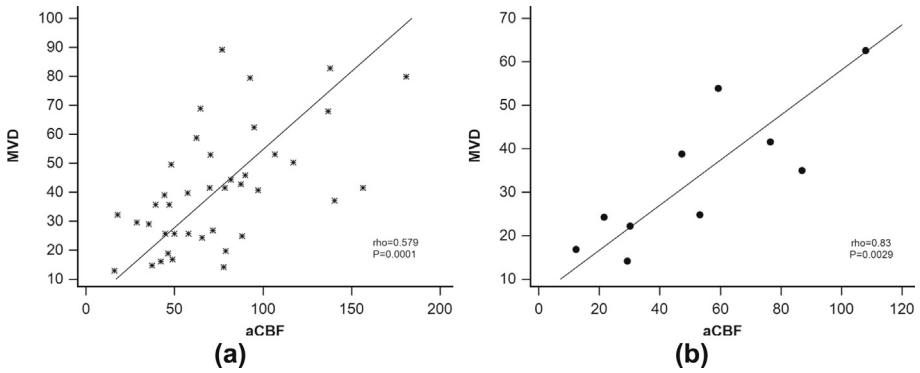

Figure 7 Scatter plots of correlations between aCBF and MVD. (a) A moderate positive correlation between aCBF on the entire enhanced proportion and MVD (rho=0.579, p=0.0001), and (b) a strong positive correlation between aCBF at the biopsy target and expression of MVD in the biopsy tissue (rho=0.83, p=0.0029).

tumors mixed with pleomorphic adenomas was revealed, progressively confirmed the essential role of MVD in determining tissue blood flow measured by ASL-MRI not matter what the tumor pathologic status.

Interestingly, when comparing aCBF and MVD based on matched ROIs, a strong positive correlation was observed. This correlation was realised by using a real-time iMRI-guided frameless stereotactic brain biopsy. This stereotactic brain biopsy technology provided real-time feedback on the biopsy needle trajectory, creating an adaptive path to the desired ROI that avoided neural structures such as the ventricle and corpus callosum. Although there are several advantages of the methods described, it is important to note potential sources of error. First, the potential error in matching centre coordinates of the target region with those of the manually drawn ROI for aCBF measurements should be considered and was set to $<$0.7 mm in this study. Second, the mean fiducial error in the desired biopsy targets between the neuro-navigational image and the anatomical image should be evaluated and was restricted to $<$1.4 mm in this study, which agrees with clinical practice. Third, to guarantee that the CBF measurements match the location of the desired biopsy target, the error in the centre coordinates between the aCBF measurement and the desired biopsy targets should be evaluated and were controlled to be no more than 6–9 mm^2 in the present study. Although this result may be biased by the small sample size (five PCNSLs and four HGGs), it emphasises the importance of tumour heterogeneity and precise radiological–pathological correlation.

There are some limitations to the present study. First, the sample size was small in this retrospective analysis, and further investigation with more patients is needed to strengthen the statistical power of the study, especially for validation of the correlation between aCBF and MVD determined through the spatial correlation of radiological and pathological measurements. Second, the assessment of necrosis for PCNSL and HGG was manually identified on CE T1WI, making the definition of atypical HGG easily susceptible to inclusion bias. To overcome this possible error, the assessment of necrosis was completed through a consensus decision by three radiologists.

In conclusion, ASL-MRI is a useful non-invasive technique for discriminating PCNSL from HGG based on aCBF and nCBF. The correlation between ASL-derived aCBF and MVD yields further insight into the underlying pathological mechanism.

Acknowledgements

This work was supported by Science and Technology Research Program for Colleges and Universities in Shandong Province (grant no. J18KB115), Research Startup Foundation of Binzhou Medical University (grant no. BY2017KYQD13), and National Natural Science Foundations of China (grant no. 81701686). The authors thank C. Yao (Department of Neurosurgery, Huashan Hospital Fudan University) for help in the technique guidance for brain biopsy. The MRI technique in this research was supported by GE Healthcare; J.Q. is employee of GE Healthcare.

Conflict of interest

The authors declare that we have no conflict of interest.

References

1. Stupp R, Mason WP, van den Bent MJ, *et al.* Radiotherapy plus concomitant and adjuvant temozolomide for glioblastoma. *N Engl J Med* 2005;**352**:987–96.
2. Schlegel U. Primary CNS lymphoma. *Ther Adv Neurol Disord* 2009;**2**:93–104.
3. Malikova H, Koubska E, Weichet J, *et al.* Can morphological MRI differentiate between primary central nervous system lymphoma and glioblastoma? *Cancer Imaging* 2016;**16**:40.
4. Alcaide-Leon P, Dufort P, Geraldo AF, *et al.* Differentiation of enhancing glioma and primary central nervous system lymphoma by texture-based machine learning. *AJNR Am J Neuroradiol* 2017;**38**:1145–50.
5. Al-Okaili RN, Krejza J, Woo JH, *et al.* Intraaxial brain masses: MR imaging–based diagnostic strategy—initial experience. *Radiology* 2007;**243**:539–50.
6. Takeuchi H, Matsuda K, Kitai R, *et al.* Angiogenesis in primary central nervous system lymphoma (PCNSL). *J Neurooncol* 2007;**84**:141–5.
7. Liao W, Liu Y, Wang X, *et al.* Differentiation of primary central nervous system lymphoma and high-grade glioma with dynamic susceptibility

contrast-enhanced perfusion magnetic resonance imaging. *Acta Radiol* 2009;**50**:217–25.
8. Kickingereder P, Sahm F, Wiestler B, *et al.* Evaluation of microvascular permeability with dynamic contrast-enhanced MRI for the differentiation of primary CNS lymphoma and glioblastoma: radiologic–pathologic correlation. *AJNR Am J Neuroradiol* 2014;**35**:1503–8.
9. Toh CH, Wei KC, Chang CN, *et al.* Differentiation of primary central nervous system lymphomas and glioblastomas: comparisons of diagnostic performance of dynamic susceptibility contrast-enhanced perfusion MR imaging without and with contrast-leakage correction. *AJNR Am J Neuroradiol* 2013;**34**:1145–9.
10. Xing Z, You RX, Li J, *et al.* Differentiation of primary central nervous system lymphomas from high-grade gliomas by rCBV and percentage of signal intensity recovery derived from dynamic susceptibility-weighted contrast-enhanced perfusion MR imaging. *Clin Neuroradiol* 2014;**24**:329–36.
11. Nakajima S, Okada T, Yamamoto A, *et al.* Differentiation between primary central nervous system lymphoma and glioblastoma: a comparative study of parameters derived from dynamic susceptibility contrast-enhanced perfusion-weighted MRI. *Clin Radiol* 2015;**70**:1393–9.
12. Lu S, Gao Q, Yu J, *et al.* Utility of dynamic contrast-enhanced magnetic resonance imaging for differentiating glioblastoma, primary central nervous system lymphoma and brain metastatic tumour. *Eur J Radiol* 2016;**85**:1722–7.
13. Lin X, Lee M, Buck O, *et al.* Diagnostic accuracy of T1-weighted dynamic contrast-enhanced MRI and DWI-ADC for differentiation of glioblastoma and primary CNS lymphoma. *AJNR Am J Neuroradiol* 2017;**38**:485–91.
14. Choi YS, Lee HJ, Ahn SS, *et al.* Primary central nervous system lymphoma and atypical glioblastoma: differentiation using the initial area under the curve derived from dynamic contrast-enhanced MR and the apparent diffusion coefficient. *Eur Radiol* 2017;**27**:1344–51.
15. Grobner T. Gadolinium—a specific trigger for the development of nephrogenic fibrosing dermopathy and nephrogenic systemic fibrosis? *Nephrol Dial Transplant* 2006;**21**:1104–8.
16. Semelka RC, Commander CW, Jay M, *et al.* Presumed gadolinium toxicity in subjects with normal renal function: a report of 4 cases. *Invest Radiol* 2016;**51**:661–5.
17. Kanda T, Fukusato T, Matsuda M, *et al.* Gadolinium-based contrast agent accumulates in the brain even in subjects without severe renal dysfunction: evaluation of autopsy brain specimens with inductively coupled plasma mass spectroscopy. *Radiology* 2015;**276**:228–32.
18. McDonald RJ, McDonald JS, Kallmes DF, *et al.* Intracranial gadolinium deposition after contrast-enhanced MR imaging. *Radiology* 2015;**275**(3):772–82.
19. Roberts DR, Lindhorst SM, Welsh CT, *et al.* High levels of gadolinium deposition in the skin of a patient with normal renal function. *Invest Radiol* 2016;**51**:280–9.
20. Lord ML, Chettle DR, Gräfe JL, *et al.* Observed deposition of gadolinium in bone using a new noninvasive *in vivo* biomedical device: results of a small pilot feasibility study. *Radiology* 2017:171161.
21. Williams DS, Detre JA, Leigh JS, *et al.* Magnetic resonance imaging of perfusion using spin inversion of arterial water. *Proc Natl Acad Sci U S A* 1992;**89**:212–6.
22. Haller S, Zaharchuk G, Thomas DL, *et al.* Arterial spin labeling perfusion of the brain: emerging clinical applications. *Radiology* 2016;**281**:337–56.
23. Lindner T, Ahmeti H, Lübbing I, *et al.* Intraoperative resection control using arterial spin labelling—proof of concept, reproducibility of data and initial results. *Neuroimage Clin* 2017;**15**:136–42.
24. Yoo RE, Choi SH, Cho HR, *et al.* Tumor blood flow from arterial spin labeling perfusion MRI: a key parameter in distinguishing high-grade gliomas from primary cerebral lymphomas, and in predicting genetic biomarkers in high-grade gliomas. *J Magn Reson Imaging* 2013;**38**:852–60.
25. Yamashita K, Yoshiura T, Hiwatashi A, *et al.* Differentiating primary CNS lymphoma from glioblastoma multiform: assessment using arterial spin labeling, diffusion-weighted imaging, and ^{18}F-fluorodeoxyglucose positron emission tomography. *Neuroradiology* 2013;**55**:135–43.
26. You SH, Yun TJ, Choi HJ, *et al.* Differentiation between primary CNS lymphoma and glioblastoma: qualitative and quantitative analysis using arterial spin labeling MR imaging. *Eur Radiol* 2018;**28**(9):3801–10. https://doi.org/10.1007/s00330-018-5359-5.
27. Weidner N. Current pathologic methods for measuring intratumoural microvessel density within breast carcinoma and other solid tumours. *Breast Cancer Res Treat* 1995;**36**:169–80.
28. Boxerman J, Schmainda K, Weisskoff R, *et al.* Relative cerebral blood volume maps corrected for contrast agent extravasation significantly correlate with glioma tumour grade, whereas uncorrected maps do not. *AJNR Am J Neuroradiol* 2016;**27**:859–67.
29. Lehmann P, Monet P, DeMarco G, *et al.* A comparative study of perfusion measurement in brain tumours at 3 Tesla MR: arterial spin labeling versus dynamic susceptibility contrast-enhanced MRI. *Eur Neurol* 2010;**64**:21–6.
30. Järnum H, Steffensen EG, Knutsson L, *et al.* Perfusion MRI of brain tumours: a comparative study of pseudo-continuous arterial spin labelling and dynamic susceptibility contrast imaging. *Neuroradiology* 2010;**52**:307–17.
31. Ningning D, Haopeng P, Xuefei D, *et al.* Perfusion imaging of brain gliomas using arterial spin labeling: correlation with histopathological vascular density in MRI-guided biopsies. *Neuroradiology* 2017;**59**:51–9.
32. Dangouloff-Ros V, Deroulers C, Foissac F, *et al.* Arterial spin labeling to predict brain tumor grading in children: correlations between histopathologic vascular density and perfusion MR imaging. *Radiology* 2016;**281**:1–14.
33. Yamamoto T, Kimura H, Hayashi K, *et al.* Pseudo-continuous arterial spin labeling MR images in Warthin tumors and pleomorphic adenomas of the parotid gland: qualitative and quantitative analyses and their correlation with histopathologic and DWI and dynamic contrast enhanced MRI findings. *Neuroradiology* 2018;**60**:803–12.